Finding Optimal Tangent Points for Reducing Distortions of Hard-label Attacks

Chen Ma [1] **Xiangyu Guo** [2] **Li Chen** [1 *] **Jun-Hai Yong** [1] **Yisen Wang** [3]
[1] School of Software, BNRist, Tsinghua University, Beijing, China
[2] Department of Computer Science and Engineering, University at Buffalo, Buffalo NY, USA
[3] Key Lab. of Machine Perception, School of EECS, Peking Univesity, Beijing, China
mac16@mails.tsinghua.edu.cn, xiangyug@buffalo.edu
{chenlee,yongjh}@tsinghua.edu.cn, yisen.wang@pku.edu.cn

Abstract

One major problem in black-box adversarial attack is the high query complexity in the hard-label attack setting, where only the top-1 predicted label is accessible. In this paper, we propose a novel geometric-based approach called Tangent Attack (TA), which identifies an optimal tangent point of a virtual hemisphere around the current adversarial example to reduce the distortion of the attack. Assuming the decision boundary is locally flat, we theoretically prove that the minimum ℓ_2 distortion can be obtained by reaching the decision boundary along the tangent line passing through such tangent point in each iteration. To improve the robustness of our method, we further propose a generalized method which replaces the hemisphere with a semi-ellipsoid to adapt to curved decision boundaries. Our approach is free of hyperparameters and pre-training. Extensive experiments conducted on the ImageNet and CIFAR-10 datasets demonstrate that our approach can consume only a small number of queries to achieve the low-magnitude distortion. The implementation source code is released online at `https://github.com/machanic/TangentAttack`.

1 Introduction

Adversarial attacks cause deep neural networks (DNNs) to make incorrect predictions by slightly perturbing benign images during the test time. They can be divided into two main categories on the basis of the amount of information exposed to the target model, namely white-box and black-box attacks. Many white-box attacks [32, 6, 29] have been proposed, and they can compute the gradients w.r.t. the target model's input images to generate adversarial examples with the first-order optimization techniques. In contrast, black-box attacks are more practical because they craft adversarial examples without requiring the target model's gradients.

Over the past years, the community has made considerable efforts in developing black-box attacks, and the proposed methods can be divided into transfer- and query-based attacks. Transfer-based attacks [25, 37, 38] generate adversarial examples by using a white-box attack method against a surrogate model to fool the target model. Although there is no need to query the target model in these attacks, the attack success rate can not be guaranteed, especially in the case of targeted attacks. To achieve satisfactory attack success rates, the query-based attacks use elaborate queries to obtain the feedback of the target model for crafting adversarial examples. In the score-based setting, the query-based attacks [2, 12, 22, 28] estimate approximate gradients by querying the predicted scores of the target model at multiple points. However, in most real-world scenarios, the score-based setting

*Corresponding author.

35th Conference on Neural Information Processing Systems (NeurIPS 2021).

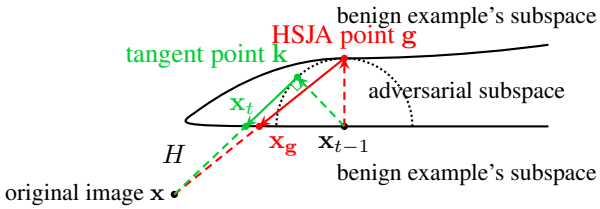

Figure 1: Simplified two-dimensional illustration of our motivation. H is the decision boundary, and $\mathbf{x}_{t-1}$ is the current adversarial example mapped onto the decision boundary at the $(t-1)$-th iteration. HSJA updates $\mathbf{x}_{t-1}$ along the gradient direction and then maps it to H at $\mathbf{x_g}$ along the line through $\mathbf{x}$ and $\mathbf{g}$. However, the optimal update should be the tangent point $\mathbf{k}$ because it can be mapped onto H at $\mathbf{x}_t$ that has the shortest distance to the original image $\mathbf{x}$.

is not applicable because the public service returns only the top-1 predicted label (*i.e.,* the hard label) rather than the predicted score. In this case, since the feedback information is limited and the objective function is discontinuous, the attack requires solving a high-dimensional combinatorial optimization problem, which is often challenging.

To reformulate the attack as a real-valued continuous optimization problem, OPT [10], Sign-OPT [11], and RayS [8] focus on minimizing an objective function $g(\theta)$, which is defined as the distance from the original image to the nearest adversarial example along the direction θ. However, when attacking complex models, it may be difficult to find a suitable direction θ along which adversarial examples exist.

Boundary Attack (BA) [4], HopSkipJumpAttack (HSJA) [7], QEBA [24], qFool [26], and Policy Driven Attack (PDA) [40] eliminate the search of the direction θ. Instead, they start from a large adversarial perturbation and then reduce its distortion while staying in the adversarial subspace. Because the output labels of the target model flip only near the decision boundary, these attacks restrict their explorations to the regions near the decision boundary. However, they do not thoroughly investigate the geometric properties of the decision boundary to accelerate the attack. For example, PDA uses a reinforcement learning framework to train a policy network to predict search directions, which are not geometrically optimal. In addition, the prediction accuracy of the policy network decreases significantly in the later stages of the iterations, resulting in worse performance of these iterations. HSJA and qFool simply use the gradient $\mathbf{u}$ estimated at the decision boundary as the direction of each update, while ignoring a geometrically critical issue, *i.e.,* $\mathbf{u}$ is not the optimal direction to be followed (Fig. 1). We could explore better search directions at each attack iteration.

To find the optimal search direction for minimizing the distortions of attack, we propose a new geometric-based approach whose motivation is illustrated in Fig. 1. We construct a virtual semicircle B centered at $\mathbf{x}_{t-1}$ to indicate all possible locations that $\mathbf{x}_{t-1}$ can move to along different directions, and the radius of B limits the range of updates for successful attacks. It is easy to observe that moving along the tangent line can reach the nearest location of the decision boundary to the original image $\mathbf{x}$, thereby producing the adversarial example with the minimum distortion. In real attack scenarios, the image data reside in a high-dimensional space, and the semicircle becomes a hemisphere. In this case, the benefit of using tangent points still exists, we provide the detailed description and the formal proof in Section 3 and appendix.

To summarize, the main contributions of this study are as follows.

1. We cast the problem of minimizing the distortion in hard-label attacks into a geometric problem. We discover that the minimum distortion can be obtained by searching the optimal tangent point of a virtual hemisphere around the adversarial example at each iteration.
2. We propose a novel geometric-based method to obtain a closed-form solution of the optimal tangent point. We provide an intuitive explanation of our approach, as well as a formal proof of its correctness.
3. To improve robustness, we further propose a generalized method that replaces the hemisphere with a semi-ellipsoid to adapt to target models with curved decision boundaries.
4. Extensive experiments conducted on the CIFAR-10 [23] and ImageNet [14] datasets demonstrate the effectiveness of our approach.

2 Related Work

Query-based black-box attacks can be divided into score- and decision-based attack (a.k.a, the hard-label attack). Score-based attacks [1–3, 9, 12, 22, 28, 31] use the predicted probability score to craft adversarial examples, which is not always available in most real-world systems. Hard-label attacks are more useful, but obviously more challenging, because only the top-1 predicted label can be obtained. The hard-label attacks usually fall into three categories.

The first category starts from the original image $\mathbf{x}_0$ and attempts to find a optimal direction θ to reach the adversarial example. OPT [10] searches an optimal θ to minimize the distance from $\mathbf{x}_0$ to the nearest adversarial example. Sign-OPT [11] improves the query efficiency of OPT by using a single query to estimate the sign of the directional derivative. RayS [8] eliminates the gradient estimation and proposes a fast check step to efficiently find the direction θ. However, RayS is only applicable to the untargeted attack under the ℓ_∞ norm constraint because it is difficult to find a suitable direction to reach the region of the target class.

The second category starts from a large perturbation or an image of the target class, and then reduces its distortion while staying in adversarial subspace, thereby gradually making it closer to the original image. BA [4] and NES [1] are two representative studies, but their query complexities are high. Biased BA [5] reinterprets BA as a biased sampling framework and incorporates different biases to improve the query efficiency. HSJA [7] utilizes the gradient estimation and binary search to achieve state-of-the-art query efficiency. HSJA can be considered the baseline of hard-label attacks. QEBA [24] improves HSJA by using dimension reduction techniques. SurFree [30] and GeoDA [33] improve HSJA by exploiting geometric properties of DNNs. However, the geometric features of DNNs have not been fully explored, and they do not support the targeted attack. PDA [40] uses a reinforcement learning framework to train a policy network to predict promising directions. However, PDA requires a high-cost pre-training, which is not always available in all tasks.

The third category uses a random sampling technique to improve query efficiency. Customized Adversarial Boundary (CAB) attack [34] uses the current noise to select the sensitive area of images and customize sampling distribution. Evolutionary [16] improves the query efficiency by reducing the dimension of the search space with the stochastic coordinate selection.

The issue of RayS and GeoDA is that they only support untargeted attacks. Because moving the original image far enough in any direction can always make it escape the benign example's subspace in untargeted attacks. However, in targeted attacks, it is difficult to find a suitable direction along which the target class's region exists. In contrast, our approach supports all types of attacks, and we exploit the geometric characteristics of the decision boundaries of DNNs to boost the attack.

3 The Proposed Approach

3.1 The Goal of Hard-label Attacks

Given a target model $f : \mathbb{R}^d \to \mathbb{R}^k$ and a benign image $\mathbf{x} \in [0,1]^d$ that is correctly classified using f, the goal of the adversary is to slightly perturb $\mathbf{x}$ into $\mathbf{x}_{\text{adv}}$, such that $f(\mathbf{x}_{\text{adv}})$ outputs incorrect prediction. In the hard-label attack, the adversary can only observe the top-1 predicted label of f, denoted as $\hat{y} = \arg\max_i f(\mathbf{x}_{\text{adv}})_i$. We define an indicator function $\phi(\cdot)$ of a successful attack:

$$\phi(\mathbf{x}_{\text{adv}}) := \begin{cases} 1 & \text{if } \hat{y} = y_{\text{adv}} \text{ in the targeted attack,} \\ & \quad \text{or } \hat{y} \neq y \text{ in the untargeted attack,} \\ 0 & \text{otherwise,} \end{cases} \tag{1}$$

where $y \in \mathbb{R}$ is the true label of $\mathbf{x}$ and $y_{\text{adv}} \in \mathbb{R}$ is a predefined target class label. In this study, we focus on generating an adversarial example $\mathbf{x}_{\text{adv}}$ that satisfies $\phi(\mathbf{x}_{\text{adv}}) = 1$, such that the distortion $d(\mathbf{x}_{\text{adv}}, \mathbf{x}) := \|\mathbf{x}_{\text{adv}} - \mathbf{x}\|_p$ is minimized. This goal can be formulated as the optimization problem:

$$\min_{\mathbf{x}_{\text{adv}}} d(\mathbf{x}_{\text{adv}}, \mathbf{x}) \quad \text{s.t. } \phi(\mathbf{x}_{\text{adv}}) = 1. \tag{2}$$

3.2 Motivation

Most recent attacks belong to the second category (Section 2) follow a common procedure: it starts from an adversarial image yet not close enough to the benign one, then it iteratively searches for a

closer adversarial image. Let us take a typical attack HSJA for example (Fig. 1). First, the attack initializes the adversarial example by using an image of the target class (in a targeted attack) or a noisy version of the original image (in an untargeted attack). Next, it performs the binary search to map the initial sample onto the decision boundary H, denoted as $\mathbf{x}_{t-1}$. Then, the algorithm iteratively performs three steps to update $\mathbf{x}_{t-1}$: **estimating gradient $\mathbf{u}$ at** H by sampling many probes around $\mathbf{x}_{t-1}$; **jumping to the point** $\mathbf{g}$ along the direction $\mathbf{u}$ with the step size determined by the geometric progression; and **mapping $\mathbf{g}$ onto** H **at** $\mathbf{x}_{\mathbf{g}}$ by performing binary search along the line passing through $\mathbf{g}$ and the original image $\mathbf{x}$. However, geometrically speaking, the estimated gradient $\mathbf{u}$ is not the optimal search direction, and we can find a better boundary point $\mathbf{x}_t$ by connecting $\mathbf{x}$ to a certain point on the semicircle B and then taking the intersection point on H. Fig. 1 shows that the tangent point $\mathbf{k}$ is the optimum update because it leads to the minimum distortion of the attack.

3.3 Definition of Optimal Tangent Points

There is some experimental evidence that the decision boundaries of DNNs are smooth surfaces with the low curvature [17, 33]. Based on this observation, we approximate the local decision boundary with a hyperplane H. Fig. 3 illustrates our problem in three-dimensional space. We will derive our algorithm from $\mathbb{R}^3$ and show that it can be directly extended to higher-dimensional spaces. Lastly, we address the case of curved decision boundaries.

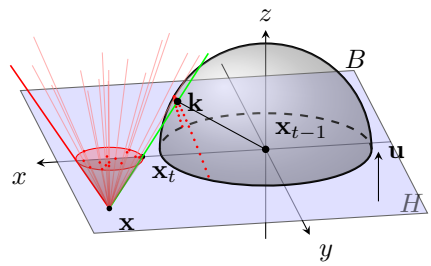

Figure 2: Geometrical explanation of Theorem 1. All points on H that are closer to $\mathbf{x}$ than $\mathbf{x}_t$ are within a red disk, which is the intersection of H and the red cone whose vertex is $\mathbf{x}$. Clearly $\mathbf{k}$ is the only intersection point of the cone and the hemisphere B. Thus, of all the lines intersecting B, only the tangent line leads to the shortest distance from $\mathbf{x}$ to H.

As described in Section 3.2, $\mathbf{x}_{t-1}$ denotes the *boundary sample* that already lies on the decision boundary. We create a virtual hemisphere B centered at $\mathbf{x}_{t-1}$ with a radius R, which is an estimation of the safe region where we can search for adversarial examples. In the targeted attack, B represents the current estimation of the target class region around $\mathbf{x}_{t-1}$. Ideally, B is small enough to be fully contained in the target class's region, *i.e.,* $\phi(\mathbf{x}') = 1$ for $\forall \mathbf{x}' \in B$. Then, we need to find a point on B which would produce the minimum distortion when mapped to H. In two-dimensional case, this point is the tangent point. However, in n-dimensional space where $n \geq 3$, there are infinitely many tangent lines of B passing through $\mathbf{x}$ which create infinitely many tangent points on B, shown as the red points in Fig. 2. Still, we will show that exactly one tangent point can lead to the minimum distortion when mapping it onto H along the tangent line.

Formally, let $\mathbf{k}$ be any point in B, $\mathbf{u}$ be the approximate gradient of H estimated at $\mathbf{x}_{t-1}$, and $\mathbf{x}_t$ be the intersection of H and the line passing through $\mathbf{x}$ and $\mathbf{k}$, we have the following theorem.

Theorem 1 *Let H, $\mathbf{u}$, $\mathbf{k}$, $\mathbf{x}$, and $\mathbf{x}_{\mathrm{t}-1}$ be defined above, then the distance $\|\mathbf{x} - \mathbf{x}_t\|$ is minimized if $\mathbf{k}$ is the optimal solution of the following constrained optimization problem:*

$$\arg\max_{\mathbf{k}} \quad \langle \mathbf{k} - \mathbf{x}_{t-1}, \mathbf{u} \rangle \tag{3}$$

$$\textit{s.t.} \quad \langle \mathbf{k} - \mathbf{x}_{t-1}, \mathbf{x} - \mathbf{k} \rangle = 0, \tag{4}$$

$$\|\mathbf{k} - \mathbf{x}_{t-1}\| = R, \tag{5}$$

$$\langle \mathbf{k} - \mathbf{x}_{t-1}, \mathbf{u} \rangle \geq 0. \tag{6}$$

In particular, the optimal $\mathbf{k}$ is in the plane spanned by $\mathbf{u}$ and $\mathbf{x} - \mathbf{x}_{t-1}$.

The objective function of Eq. (3) is to maximize the projection of the vector $\mathbf{k} - \mathbf{x}_{t-1}$ onto $\mathbf{u}$, which is equivalent to finding $\mathbf{k}$ that is farthest away from H. The first constraint ensures that $\mathbf{k}$ is a tangent point. The second constraint indicates $\mathbf{k}$ is on the surface of B. The last constraint states that $\mathbf{k}$ cannot appear on the same side of H as $\mathbf{x}$, which is always satisfied if $\|\Pi_H(\mathbf{x} - \mathbf{x}_{t-1})\| \geq R$, where the notation $\Pi_H : \mathbb{R}^n \mapsto H$ denotes the orthogonal projection from $\mathbb{R}^n$ onto the hyperplane H. If there is no feasible solution, then our algorithm (Algorithm 1) reduces the radius R to guarantee that the last constraint is always satisfied. The formal proof of Theorem 1 is presented in the appendix. Here, we refer the readers to Fig. 2 for an intuitive geometrical explanation. Eq. (3) is computationally

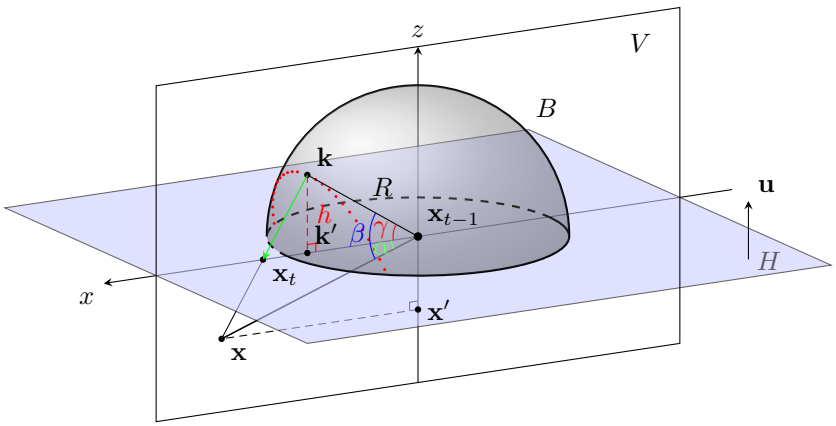

Figure 3: The illustration of the optimal tangent point $\mathbf{k}$ for the flat decision boundary. The tangent point $\mathbf{k}$ is on the surface of a virtual hemisphere B with a radius R centered at the adversarial example $\mathbf{x}_{t-1}$. $\mathbf{x}$ is the original image, $\mathbf{x}_t$ is the intersection point of the tangent line and the decision hyperplane H, $\mathbf{k}'$ and $\mathbf{x}'$ are the orthogonal projections of $\mathbf{k}$ and $\mathbf{x}$ onto H and z axis, respectively.

expensive to solve in the high-dimensional space. Fortunately, we show there actually exists a closed-form solution.

3.4 Closed-Form Solution of the Optimal Tangent Point

The main intuition of the derivation is illustrated in Fig. 3, which shows an example in $\mathbb{R}^3$. For ease of presentation, we move $\mathbf{x}_{t-1}$ to $\mathbf{0}$. The known variables are $\mathbf{x}$, $\mathbf{x}_{t-1}$, the unit normal vector $\mathbf{u}$ of hyperplane H, and the radius R. We need to solve for the unknown $\mathbf{k}$. Let $V = \text{span}(\{\mathbf{x}, \mathbf{u}\})$ be the *plane* spanned by $\mathbf{x}$ and $\mathbf{u}$. According to Theorem 1, we know $\mathbf{k} \in V$. Let us denote the angle between $\mathbf{x}$ and H as α, the angle between $\mathbf{x}$ and $\mathbf{k}$ as β, and the angle between $\mathbf{k}$ and H as γ. Then, $\beta = \alpha + \gamma$ because all three points $\mathbf{x}$, $\mathbf{k}$, and $\mathbf{x}_{t-1}$ are on the same plane V. Because the angle between $\mathbf{x}$ and $\mathbf{u}$ is $\pi \,/\, 2 + \alpha$, we have

$$\langle \mathbf{x}, \mathbf{u} \rangle = \|\mathbf{x}\| \cdot \|\mathbf{u}\| \cdot \cos(\frac{\pi}{2} + \alpha) = \|\mathbf{x}\| \cdot \|\mathbf{u}\| \cdot (-\sin\alpha)\,. \tag{7}$$

Then we have $\sin\alpha = -\frac{\langle \mathbf{x}, \mathbf{u} \rangle}{\|\mathbf{x}\| \cdot \|\mathbf{u}\|}$ and $\cos\alpha = \sqrt{1 - \sin^2\alpha} = \frac{\sqrt{\|\mathbf{x}\|^2 \cdot \|\mathbf{u}\|^2 - (\langle \mathbf{x}, \mathbf{u} \rangle)^2}}{\|\mathbf{x}\| \cdot \|\mathbf{u}\|}$. By constraint (4), $\mathbf{x} - \mathbf{k}$ is orthogonal to $\mathbf{k}$. Thus, we have $\cos\beta = R \,/\, \|\mathbf{x}\|$ and $\sin\beta = \sqrt{1 - \cos^2\beta} = \sqrt{\|\mathbf{x}\|^2 - R^2} \,/\, \|\mathbf{x}\|$. Then $\sin\gamma$ and $\cos\gamma$ can be derived as functions of α and β from basic facts of trigonometric functions:

$$\begin{aligned} \sin\gamma &= \sin(\beta - \alpha) = \sin\beta\cos\alpha - \cos\beta\sin\alpha, \\ \cos\gamma &= \cos(\beta - \alpha) = \cos\beta\cos\alpha + \sin\beta\sin\alpha. \end{aligned} \tag{8}$$

Now, let $\mathbf{k}' \in H$ be the orthogonal projection of $\mathbf{k}$ onto the plane H. The distance between $\mathbf{k}$ and $\mathbf{k}'$ is denoted as h (Fig. 3). Then $h = R \cdot \sin\gamma = R \cdot (\sin\beta\cos\alpha - \cos\beta\sin\alpha)$.

To derive $\mathbf{k}'$, let us denote $\mathbf{x}'$ as the orthogonal projection of $\mathbf{x}$ onto z axis. So we have $\mathbf{x}' = \langle \mathbf{x}, -\mathbf{u} \rangle \cdot (-\mathbf{u}) \,/\, \|\mathbf{u}\|^2 = \langle \mathbf{x}, \mathbf{u} \rangle \cdot \mathbf{u} \,/\, \|\mathbf{u}\|^2$. Then, because $\mathbf{k}'$ and $\mathbf{x} - \mathbf{x}'$ are on the same direction, we have

$$\frac{\mathbf{k}'}{\|\mathbf{k}'\|} = \frac{\mathbf{x} - \mathbf{x}'}{\|\mathbf{x} - \mathbf{x}'\|}. \tag{9}$$

Now, $\|\mathbf{k}'\| = R \cdot \cos\gamma$ and $\mathbf{x}' = \langle \mathbf{x}, \mathbf{u} \rangle \cdot \mathbf{u} \,/\, \|\mathbf{u}\|^2$ are plugged into Eq. (9), and $\mathbf{k}'$ is obtained as

$$\mathbf{k}' = \frac{\mathbf{x} - \mathbf{x}'}{\|\mathbf{x} - \mathbf{x}'\|} \cdot \|\mathbf{k}'\| = \frac{\mathbf{x} - \langle \mathbf{x}, \mathbf{u} \rangle \cdot \mathbf{u} \,/\, \|\mathbf{u}\|^2}{\|\mathbf{x} - \langle \mathbf{x}, \mathbf{u} \rangle \cdot \mathbf{u} \,/\, \|\mathbf{u}\|^2\|} \cdot R \cdot \cos\gamma. \tag{10}$$

Therefore, $\mathbf{k}$ can be derived as

$$\mathbf{k} = \mathbf{k}' + h \cdot \mathbf{u} = \frac{\mathbf{x} - \langle \mathbf{x}, \mathbf{u} \rangle \cdot \mathbf{u} \,/\, \|\mathbf{u}\|^2}{\|\mathbf{x} - \langle \mathbf{x}, \mathbf{u} \rangle \cdot \mathbf{u} \,/\, \|\mathbf{u}\|^2\|} \cdot R \cdot \cos\gamma + h \cdot \mathbf{u}. \tag{11}$$

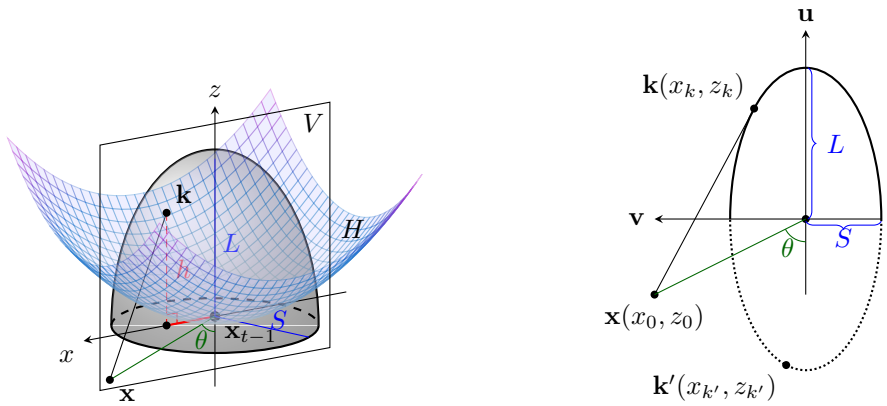

(a) 3D view of Generalized Tangent Attack

(b) 2D plane V spanned by $\mathbf{x}$ and $\mathbf{u}$.

Figure 4: Illustration of the derivation of Generalized Tangent Attack, which replaces the hemisphere B with a semi-ellipsoid to increase the height of $\mathbf{k}$ to adapt to curved decision boundaries.

Finally, because $\mathbf{x}_{t-1}$ has been moved to the origin, we need to move $\mathbf{k}$ back by adding $\mathbf{x}_{t-1}$.

We remark that although the above derivation is illustrated in $\mathbb{R}^3$, it can be directly applied to higher dimensions. The reason is Theorem 1, which essentially reduces any dimension space to $\mathbb{R}^2$: to find the optimal $\mathbf{k}$, we only need to focus on the plane V spanned by $\mathbf{u}$ and $\mathbf{x} - \mathbf{x}_{t-1}$.

3.5 Generalized Tangent Attack

When the local decision boundary is not flat enough, the boundary point obtained via the tangent line may not be the optimal, as shown in Fig. 4a. A simple solution is to simply continue halving the radius R of the hemisphere: as long as R becomes small enough, the local flatness can always be obtained. However, too small a radius will reduce the convergence rate of our algorithm, because the distance between $\mathbf{x}_t$ and $\mathbf{x}_{t-1}$ is proportional to R. Therefore, when the classification decision boundary is a curved surface, the attack algorithm should change the shape of hemisphere rather than simply reducing R. Based on this idea, we propose the Generalized Tangent Attack (G-TA).

First, although the shape of the decision boundary can be very complex in a high-dimensional space, the important thing for our algorithm is only the situation in the two-dimensional plane spanned by $\mathbf{x}$ and $\mathbf{u}$. In particular, if the decision boundary is "downward" curved (as opposed to the example in Fig. 4a), then searching along the tangent line is still a better approach than HSJA's solution. Thus, the only "bad case" we have to deal with is when the decision boundary is "upward" curved and has a large curvature, as shown in Fig. 4a.

According to Theorem 1, we only need to focus on the plane V spanned by $\mathbf{x}$ and $\mathbf{u}$, as shown in Fig. 4b. Now, $\mathbf{u}$ and $\mathbf{v} := (\mathbf{x} - \langle \mathbf{x}, \mathbf{u} \rangle \cdot \mathbf{u} \,/\, \|\mathbf{u}\|^2) \,/\, \|\mathbf{x} - \langle \mathbf{x}, \mathbf{u} \rangle \cdot \mathbf{u} \,/\, \|\mathbf{u}\|^2\|$ form an orthogonal basis of the plane V, then $\mathbf{x}$ can be identified with coordinates (x_0, z_0), *i.e.,* $\mathbf{x} = x_0\mathbf{v} + z_0\mathbf{u}$. Let θ denote the angle between the vector $\mathbf{x}$ and the vector $-\mathbf{u}$, *i.e.,* $\theta = \arccos(\frac{\langle \mathbf{x}, -\mathbf{u} \rangle}{\|\mathbf{x}\| \cdot \|\mathbf{u}\|})$. Then $(x_0, z_0) = (\|\mathbf{x}\| \cdot \sin\theta, -\|\mathbf{x}\| \cdot \cos\theta)$. Consider the projection of the ellipsoid on V (which is a ellipse), we denote L as its radius along the direction of $\mathbf{u}$, and S as its radius along the direction of $\mathbf{v}$. Because the optimal tangent point $\mathbf{k}$ lies in the plane V, $\mathbf{k}$ can also be identified as $\mathbf{k} = x_k\mathbf{v} + z_k\mathbf{u}$, and we only need to solve for the unknown (x_k, z_k).

The ellipse is characterized by the equation $x^2 \,/\, S^2 + z^2 \,/\, L^2 = 1$, thus the tangent point $\mathbf{k}$ satisfies $x_k^2 \,/\, S^2 + z_k^2 \,/\, L^2 = 1$. Now we view z as a function of x, and take the derivative w.r.t. x at both sides of the equation to get the following formula:

$$\frac{2x_k}{S^2} + \frac{2z_k}{L^2} \cdot \frac{dz}{dx}\bigg|_{x=x_k} = 0. \tag{12}$$

Thus, we have the slope of tangent line at $\mathbf{k}$ be $\frac{dz}{dx}\big|_{x=x_k} = -\frac{x_k L^2}{z_k S^2}$. Therefore, the tangent line can be written as $z - z_k = -\frac{x_k L^2}{z_k S^2}(x - x_k)$. Since the tangent line passes through $\mathbf{x}$, we know

$z_0 - z_k = -\frac{x_k L^2}{z_k S^2}(x_0 - x_k)$. In summary, we can obtain the following system of equations:

$$\begin{cases} L^2 x_k^2 + S^2 z_k^2 - x_k x_0 L^2 - z_0 z_k S^2 = 0, \\ \dfrac{x_k^2}{S} + \dfrac{z_k^2}{L} = 1. \end{cases} \tag{13}$$

In Eq. (13), the known variables are L, S, x_0 and z_0, and the unknown variables that we need to solve for are x_k and z_k. In general, there are two solutions for Eq. (13), *i.e.,* $\mathbf{k}$ and $\mathbf{k}'$ depicted in Fig. 4b. Apparently, the solution of the optimal tangent point should satisfy $z_k > 0$, so the one of two solutions in which $z_k > 0$ should be picked:

$$\begin{cases} x_k = \dfrac{S^2 \left(L^2 - z_0 \cdot \frac{L^2 S^2 z_0 + L^2 x_0 \sqrt{-L^2 S^2 + L^2 x_0^2 + S^2 z_0^2}}{L^2 x_0^2 + S^2 z_0^2} \right)}{L^2 \cdot x_0}, \\ z_k = \dfrac{L^2 S^2 z_0 + L^2 x_0 \sqrt{-L^2 S^2 + L^2 x_0^2 + S^2 z_0^2}}{L^2 x_0^2 + S^2 z_0^2}. \end{cases} \tag{14}$$

Finally, the optimal tangent point $\mathbf{k}$ is obtained via $\mathbf{k} = |x_k| \cdot \frac{\mathbf{x} - \langle \mathbf{x}, \mathbf{u} \rangle \cdot \mathbf{u} / \|\mathbf{u}\|^2}{\|\mathbf{x} - \langle \mathbf{x}, \mathbf{u} \rangle \cdot \mathbf{u} / \|\mathbf{u}\|^2\|} + z_k \cdot \mathbf{u}$. In the implementation, the value of L is determined in the same way as the radius R in TA (the hemisphere version). So we fix $L = R$, and use a hyperparameter $r = L/S$ to control the value of S. Imagine that in the case of $\mathbb{R}^3$, the semi-ellipsoid becomes "slender" by setting $r > 1$, thereby adapting to the decision boundary of curved surface while preserving a relatively large step size.

3.6 The Complete Algorithm

TA and G-TA can be combined into one algorithm process, which is shown in Algorithm 1. It first performs a binary search to map the initial sample $\tilde{\mathbf{x}}_0$ to the decision boundary. Note that the binary search step always maps any $\mathbf{x}_{\text{adv}}$ to the adversarial side of H that satisfies $\phi(\mathbf{x}_{\text{adv}}) = 1$, hence the attack success rate is always 100%. Then, it performs a *for* loop of T iterations to find the adversarial example that is close to $\mathbf{x}$. In the first iteration, we sample B_0 probes around the boundary sample to estimate the gradient, which is increased to $B_0\sqrt{t}$ at the t-th iteration. This is because the error of gradient estimation in the later iterations has a greater impact on the attack performance, so using more samples can reduce the estimation error. Then, a *while* loop is performed to determine a reasonable radius R by repeatedly halving the radius until the tangent point $\mathbf{k}$ is in the adversarial subspace. Finally, Algorithm 1 uses the binary search method to map $\mathbf{k}$ back to the classification decision boundary to end this iteration.

Algorithm 1 Tangent Attack

Input: benign image $\mathbf{x}$, attack success indicator function $\phi(\cdot)$ defined in Eq. (1), initial batch size B_0, iteration T, mode $m \in \{$semi-ellipsoid, hemisphere$\}$, radius ratio r.
Initialize $\tilde{\mathbf{x}}_0$ that satisfies $\phi(\tilde{\mathbf{x}}_0) = 1$;
$\mathbf{x}_0 \leftarrow$ BinarySearch$(\tilde{\mathbf{x}}_0, \mathbf{x}, \phi)$; ▷ boundary search
$d_0 = \|\mathbf{x}_0 - \mathbf{x}\|_2$;
for t **in** $0, \ldots, T-1$ **do**
  Sample $B_t \leftarrow B_0\sqrt{t}$ random vectors to estimate the gradient $\mathbf{u}$;
  Initialize $R \leftarrow d_{t-1}/\sqrt{t}$; ▷ the initial radius
  while true do
    Compute the optimal tangent point $\mathbf{k}$ based on Eq. (11) **if** $m =$ hemisphere **else** Eq. (14)
    $R \leftarrow \frac{R}{2}$; ▷ search the radius, and we set $L = R, S = \frac{L}{r}$ if $m =$ semi-ellipsoid
    if $\phi(\mathbf{k}) = 1$ **then**
      break;
    end if
  end while
  $\mathbf{k} \leftarrow$ Clip$(\mathbf{k}, 0, 1)$;
  $\mathbf{x}_t \leftarrow$ BinarySearch$(\mathbf{k}, \mathbf{x}, \phi)$; ▷ boundary search
  $d_t = \|\mathbf{x}_t - \mathbf{x}\|_2$.
end for

4 Experiment

4.1 Experimental Setting

Datasets. TA and G-TA are evaluated on two datasets, namely CIFAR-10 and ImageNet with the image resolutions of $32 \times 32 \times 3$ and $299 \times 299 \times 3$, respectively. We randomly select $1{,}000$ correctly classified images from their validation sets for experiments.

Method Setting. The initial batch size B_0 is set to 100, which means the algorithm samples 100 probes for estimating gradient at the first iteration. The threshold γ that controls the termination of the binary search is set to 1.0 in the CIFAR-10 dataset and $1{,}000$ in the ImageNet dataset. The radius ratio r is set to 1.5 in the CIFAR-10 dataset and 1.1 in the ImageNet dataset. Besides, we also set r to 1.5 when attacking defense models. In targeted attacks, the target class label is set to $y_{adv} = (y + 1) \mod C$, where y is the true label, and C is the number of classes.

Compared Methods. The advantage of our method is that it supports all types of attacks, including both untargeted and targeted attacks under ℓ_2 norm and ℓ_∞ norm constraints. Therefore, for complete and fair comparisons, we select the compared methods that support both untargeted and targeted attacks with state-of-the-art performance, including Boundary Attack (BA) [4], Sign-OPT [11], SVM-OPT [11], and HopSkipJumpAttack (HSJA) [7]. HSJA is adopted as the baseline, whose hyperparameters are set to be the same with ours (*e.g,* the same initial batch size B_0 and threshold γ). In addition, QEBA [24] is a HSJA-based method which has three variants: QEBA-I, QEBA-S and QEBA-F. We select QEBA-S in the additional experiment to verify whether the proposed method can improve attack performance of other HSJA-based method. For the consistency of experiments, we translate the implementations of Sign-OPT, SVM-OPT and HSJA from the official NumPy version into the PyTorch version by replacing each NumPy function with the corresponding PyTorch function. Thus, the two versions behave exactly the same. In the targeted attack, we randomly select an image from the target class of the validation set to be the initial sample of HSJA, BA, TA and G-TA. For fair comparison, we set the initial direction θ_0 of Sign-OPT and SVM-OPT to the direction of a randomly selected image of the target class. The detailed settings are presented in the appendix.

Target Models. In the CIFAR-10 dataset, we select four target models from the PyTorch-Classification package[2]: (1) a 272-layer PyramidNet+ShakeDrop network (PyramidNet-272) [19, 39] trained using AutoAugment [13] ; (2) a model obtained through a neural architecture search called GDAS [15]; (3) a wide residual network with 28 layers and 10 times width expansion (WRN-28) [41]; and (4) a wide residual network with 40 layers (WRN-40) [41]. In the ImageNet dataset, we select four target models from the pre-trained models package[3]: (1) Inception-v3 [36], (2) Inception-v4 [35], (3) ResNet-101 [20], and (4) SENet-154 [21].

Evaluation Metric. Following previous studies [40], we report the mean ℓ_2 distortions as $\frac{1}{|\mathbf{X}|}\sum_{\mathbf{x}\in\mathbf{X}}(\|\mathbf{x}_{\text{adv}} - \mathbf{x}\|_2)$ under different query budgets, where $\mathbf{X}$ is the test set.

4.2 Comparisons with State-of-the-Art Methods

Results of Attacks against Undefended Models. Tables 1 and 2 show the experimental results on the ImageNet and CIFAR-10 datasets. We derive two conclusions based on the results:

(1) We found that the experiments of CIFAR-10 requires a larger radius ratio r than that of ImageNet to achieve the satisfactory performance of G-TA. We speculate that the reason is that the target models of ImageNet have relatively flat decision boundaries.

(2) TA is more effective in targeted attacks, while the G-TA performs better in untargeted ones. This is because the adversarial subspace in the target attack is narrower and more scattered, making the local classification decision boundary smoother, so that Theorem 1 holds and TA performs better.

In addition, one unique benefit of our approach is that it can be used as a performance enhanced plug-in when combining it with other HSJA-based approaches (*e.g.*, QEBA-S). Specifically, the method is to change the jump directions of boundary samples of QEBA-S to the directions of the optimal tangent points. We present that "QEBA-S + TA" can further improve the performance of QEBA-S, as shown in Table 3.

[2]Pre-trained weights: `https://github.com/bearpaw/pytorch-classification`

[3]Pre-trained weights: `https://github.com/Cadene/pretrained-models.pytorch`

Table 1: Mean ℓ_2 distortions of different query budgets on the ImageNet dataset, where $r = 1.1$.

Target Model	Method	Targeted Attack						Untargeted Attack					
		@300	@1K	@2K	@5K	@8K	@10K	@300	@1K	@2K	@5K	@8K	@10K
Inception-v3	BA [4]	111.798	108.044	106.283	102.715	86.931	78.326	-	107.558	102.309	95.776	78.668	60.296
	Sign-OPT [11]	103.939	87.706	71.291	46.744	34.640	29.414	121.085	79.158	43.642	16.625	10.557	8.680
	SVM-OPT [11]	**101.630**	82.950	67.965	46.275	35.694	31.106	121.135	66.027	36.763	15.736	10.501	8.789
	HSJA [7]	111.562	95.295	82.111	52.544	37.395	30.425	103.605	57.295	37.185	15.484	9.989	7.967
	TA	103.781	**80.327**	**66.708**	**42.121**	**30.846**	**25.566**	94.752	52.523	35.229	15.040	9.748	7.793
	G-TA	103.724	81.089	67.168	42.434	31.011	25.587	**94.668**	**52.037**	**34.540**	**14.643**	**9.540**	**7.618**
Inception-v4	BA [4]	110.343	106.616	104.586	100.321	84.058	75.507	-	116.075	111.474	104.451	86.572	66.283
	Sign-OPT [11]	101.620	85.731	69.719	46.416	34.957	30.004	132.991	86.431	48.292	18.678	11.567	9.262
	SVM-OPT [11]	**99.856**	81.342	66.982	45.667	35.477	31.152	132.227	72.920	41.095	17.611	11.418	9.372
	HSJA [7]	109.670	93.916	80.937	52.358	37.773	30.958	110.727	63.731	42.290	17.936	11.367	8.911
	TA	101.666	**78.683**	**65.304**	**41.629**	30.993	25.958	101.207	58.616	40.314	17.639	11.304	8.907
	G-TA	101.495	79.210	65.888	42.002	**30.965**	**25.847**	**101.173**	**58.225**	**39.788**	**17.265**	**11.008**	**8.677**
SENet-154	BA [4]	81.090	77.723	76.122	71.967	55.953	47.652	-	75.998	71.671	66.983	53.917	40.725
	Sign-OPT [11]	75.722	62.876	49.191	30.155	21.333	17.672	70.035	47.705	27.314	10.890	6.643	5.245
	SVM-OPT [11]	74.658	58.677	46.827	30.264	22.461	19.186	69.854	40.291	**23.692**	10.494	6.666	5.409
	HSJA [7]	77.035	63.488	51.802	30.138	19.680	16.261	71.248	38.035	24.895	10.218	5.855	4.842
	TA	70.739	55.256	**43.694**	**24.961**	**16.756**	**13.876**	**65.589**	**35.689**	24.037	10.039	5.774	4.766
	G-TA	**70.591**	**55.224**	44.047	25.041	16.854	14.047	65.871	35.768	23.954	**9.959**	**5.733**	**4.734**
ResNet-101	BA [4]	81.565	77.903	76.366	72.392	58.746	51.679	-	64.007	60.389	56.544	44.175	31.371
	Sign-OPT [11]	76.732	63.939	51.231	32.439	23.160	19.248	56.244	38.282	21.985	10.048	7.050	6.050
	SVM-OPT [11]	77.031	61.417	49.842	32.806	24.553	20.964	55.894	32.638	19.409	9.830	7.185	6.281
	HSJA [7]	76.121	63.091	52.301	31.018	20.472	16.911	56.264	27.443	17.717	7.649	4.723	**4.019**
	TA	**72.434**	**57.969**	**47.142**	**27.699**	**18.788**	**15.414**	53.197	26.777	17.651	7.730	4.822	4.107
	G-TA	72.459	58.320	47.297	27.905	19.045	15.633	**53.058**	**26.631**	**17.384**	**7.602**	**4.720**	4.026

Table 2: Mean ℓ_2 distortions with different query budgets on the CIFAR-10 dataset, where $r = 1.5$.

Target Model	Method	Targeted Attack						Untargeted Attack					
		@300	@1K	@2K	@5K	@8K	@10K	@300	@1K	@2K	@5K	@8K	@10K
PyramidNet-272	BA [4]	8.651	8.073	8.013	6.387	4.189	3.333	-	5.636	4.725	4.414	2.750	1.696
	Sign-OPT [11]	8.279	6.331	4.250	1.718	0.960	0.718	4.387	2.334	1.178	0.403	0.267	0.226
	SVM-OPT [11]	9.207	6.801	4.530	2.010	1.207	0.947	4.481	2.318	1.093	0.414	0.276	0.236
	HSJA [7]	7.917	4.329	2.523	**0.793**	**0.489**	**0.397**	4.505	1.279	0.713	0.333	0.255	0.227
	TA	7.943	**4.267**	2.488	0.809	0.503	0.406	**4.256**	1.275	0.710	0.329	0.253	0.226
	G-TA	**7.816**	4.277	**2.469**	0.803	0.505	0.412	4.432	**1.270**	**0.702**	**0.329**	**0.252**	**0.225**
GDAS	BA [4]	8.487	7.885	7.821	6.034	3.632	2.703	-	2.717	2.514	2.373	1.642	1.106
	Sign-OPT [11]	8.372	6.514	4.351	1.827	0.987	0.711	4.917	4.159	3.260	1.352	0.452	0.250
	SVM-OPT [11]	9.529	7.243	5.092	2.347	1.317	0.958	4.909	3.950	2.736	1.082	0.371	0.234
	HSJA [7]	7.714	3.566	1.966	0.591	0.365	0.301	2.188	0.756	0.483	0.261	0.208	0.189
	TA	**7.674**	**3.529**	**1.946**	0.585	0.366	0.302	2.190	0.774	0.485	0.257	0.206	0.187
	G-TA	7.697	3.558	1.959	**0.583**	**0.361**	**0.298**	**2.161**	**0.745**	**0.476**	**0.255**	**0.204**	**0.185**
WRN-28	BA [4]	8.688	8.046	7.984	5.786	2.486	1.555	-	4.425	3.648	3.435	1.543	0.832
	Sign-OPT [11]	8.258	5.576	3.260	1.087	0.593	0.459	3.093	1.494	0.828	0.319	**0.239**	**0.213**
	SVM-OPT [11]	9.516	5.968	3.744	1.367	0.728	0.553	2.977	1.466	0.723	0.325	0.245	0.221
	HSJA [7]	6.810	2.603	1.326	0.518	0.389	0.347	3.052	0.797	0.508	0.299	0.250	0.232
	TA	6.802	2.556	1.311	0.519	0.394	0.353	**2.974**	0.785	**0.496**	**0.293**	0.249	0.233
	G-TA	**6.755**	**2.543**	**1.281**	**0.513**	**0.387**	**0.345**	2.995	**0.782**	0.502	0.298	0.250	0.232
WRN-40	BA [4]	8.658	8.014	7.953	5.738	2.484	1.566	-	4.377	3.586	3.367	1.487	0.821
	Sign-OPT [11]	8.156	5.579	3.300	1.186	0.646	0.501	4.754	3.239	1.885	0.311	**0.226**	**0.201**
	SVM-OPT [11]	9.339	6.061	3.840	1.445	0.800	0.605	4.457	2.756	0.739	0.310	0.229	0.206
	HSJA [7]	6.909	2.648	1.330	0.528	0.400	**0.357**	2.992	0.777	0.498	0.290	0.242	0.225
	TA	6.944	**2.579**	**1.295**	**0.523**	**0.398**	0.358	**2.926**	**0.770**	**0.490**	0.288	0.243	0.227
	G-TA	**6.783**	2.605	1.320	0.535	0.403	0.361	2.952	0.772	0.492	**0.288**	0.241	0.223

Table 3: Experimental results of the combined method of QEBA-S and TA.

Target Model	Method	Targeted Attack					
		@300	@1K	@2K	@5K	@8K	@10K
Inception-v3	QEBA-S [24]	**100.295**	79.604	63.621	35.194	22.773	18.414
	QEBA-S + TA	104.490	**75.622**	**59.836**	**33.112**	**22.329**	**17.799**
Inception-v4	QEBA-S [24]	**97.772**	77.347	62.451	35.275	23.204	19.002
	QEBA-S + TA	101.845	**73.838**	**58.554**	**33.288**	**23.160**	**18.736**
SENet-154	QEBA-S [24]	**72.831**	55.367	42.674	21.988	13.888	11.210
	QEBA-S + TA	76.547	**52.269**	**39.740**	**20.608**	**13.873**	**11.016**
ResNet-101	QEBA-S [24]	**75.567**	57.929	44.983	23.209	14.402	11.467
	QEBA-S + TA	78.709	**53.917**	**41.245**	**21.198**	**13.856**	**10.773**

Results of Attacks against Defense Models. We conduct the experiments of untargeted attacks on defense models. Fig. 5 shows the experimental results on the CIFAR-10 dataset. We select 4 defense models: (1) a model obtained through adversarial training, abbreviated as AT [29]; (2) an

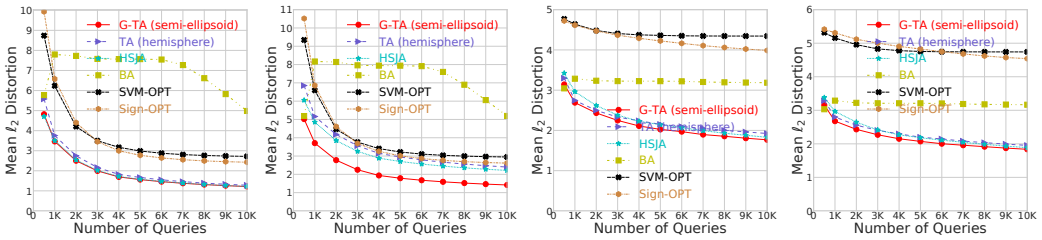

(a) AT ($\epsilon = 8/255$) (b) TRADES ($\epsilon = 8/255$) (c) JPEG (d) Feature Distillation

Figure 5: Experimental results of the attacks against defense models with the backbone of ResNet-50.

improved AT that optimizes a regularized surrogate loss, named as TRADES [42]; (3) an image-transformation-based defense called JPEG [18]; and (4) a DNN-oriented compression defense called Feature Distillation [27]. All defense models adopt ResNet-50 as the backbone. Previous studies [43] have shown that AT and TRADES have the issue of robust overfitting, which leads to a significant increase in the curvature of the classification decision boundary. Fig. 5b shows that G-TA performs best in attacking TRADES. This superiority is also demonstrated in attacks on other defenses (*e.g.*, Fig. 5d), proving the effectiveness of G-TA in attacking the models with curved decision boundaries.

4.3 Comprehensive Understanding of Tangent Attack

In the ablation studies, we conduct the experiments of the targeted attacks on the ImageNet dataset to understand our approach in depth, and the target model is ResNet-50. The results are shown in Fig. 6.

Initialization. Our algorithm starts with an image $\tilde{\mathbf{x}}_0$ selected from the target class, and we study three selection strategies: (1) a randomly selected image, (2) the image with the shortest distance to the original image, and (3) the image with the longest distance to the original image. Fig. 6a shows that the strategy of (2) achieves the best performance.

Radius Ratio. Fig. 6b shows that the performance is not sensitive to the radius ratio r of G-TA.

Jump Direction. Fig. 6c shows the effects of different jump directions. RandomHSJA is a variant of HSJA which adopts a random vector $\mathbf{r}$ that satisfies $\langle \mathbf{r}, \mathbf{u} \rangle > 0$ as the jump direction. Fig. 6c verifies the benefit of jumping to the optimal tangent point.

Initial Batch Size. In general, Fig. 6d shows that a smaller B_0 performs better since it saves queries. But $B_0 = 5$ performs worse than $B_0 = 30$ because it uses too few samples for gradient estimation.

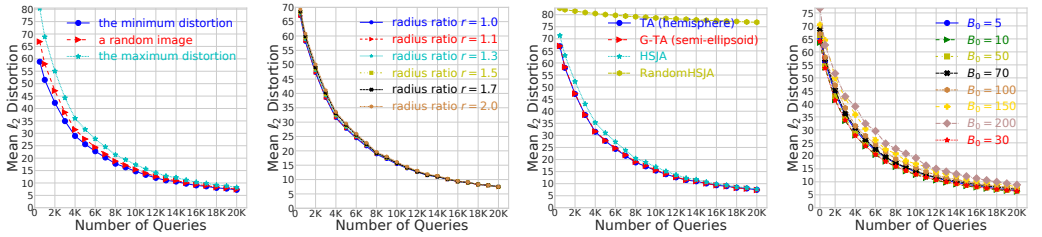

(a) initial $\tilde{\mathbf{x}}_0$ selection (b) radius ratio (c) jump directions (d) initial batch size B_0

Figure 6: Experimental results of ablation studies.

5 Conclusion

In this paper, we propose a new geometric-based method for query-efficient hard-label black-box attacks. Our method relies on the observation that the minimum ℓ_2 distortion can be obtained by searching a boundary point along a tangent line of a virtual hemisphere. We offer a closed-form solution for computing the optimal tangent point and provide a formal proof of its correctness. We further propose a generalized method that replaces the hemisphere to a semi-ellipsoid to adapt to the target models with curved decision boundaries. Lastly, we evaluate our approach through extensive experiments and show its superior performance compared with baseline methods.

Acknowledgments

This research is partially supported by the National Key R&D Program of China (2019YFB1405703) and TC190A4DA/3, the National Natural Science Foundation of China (Grant Nos. 62021002, 61972221). Yisen Wang is partially supported by the National Natural Science Foundation of China under Grant 62006153, and Project 2020BD006 supported by PKU-Baidu Fund.

References

[1] Ilyas Andrew, Engstrom Logan, Athalye Anish, and Lin Jessy. Black-box adversarial attacks with limited queries and information. In *International Conference on Machine Learning*, pages 2142–2151, 2018.

[2] Yang Bai, Yuyuan Zeng, Yong Jiang, Yisen Wang, Shu-Tao Xia, and Weiwei Guo. Improving query efficiency of black-box adversarial attack. In *European Conference on Computer Vision*, pages 101–116, 2020.

[3] Arjun Nitin Bhagoji, Warren He, Bo Li, and Dawn Song. Practical black-box attacks on deep neural networks using efficient query mechanisms. In *European Conference on Computer Vision*, pages 158–174, 2018.

[4] Wieland Brendel, Jonas Rauber, and Matthias Bethge. Decision-based adversarial attacks: reliable attacks against black-box machine learning models. In *International Conference on Learning Representations*, pages 1–12, 2018.

[5] T. Brunner, F. Diehl, M. T. Le, and A. Knoll. Guessing smart: biased sampling for efficient black-box adversarial attacks. In *IEEE/CVF International Conference on Computer Vision*, pages 4957–4965, 2019.

[6] Nicholas Carlini and David A. Wagner. Towards evaluating the robustness of neural networks. In *IEEE Symposium on Security and Privacy*, pages 39–57, 2017.

[7] Jianbo Chen, Jordan Michael I., and Wainwright Martin J. HopSkipJumpAttack: a query-efficient decision-based adversarial attack. In *IEEE Symposium on Security and Privacy*, pages 1277–1294, 2020.

[8] Jinghui Chen and Quanquan Gu. RayS: a ray searching method for hard-label adversarial attack. In *ACM SIGKDD International Conference on Knowledge Discovery and Data Mining*, page 1739–1747, 2020.

[9] Pin-Yu Chen, Huan Zhang, Yash Sharma, Jinfeng Yi, and Cho-Jui Hsieh. ZOO: zeroth order optimization based black-box attacks to deep neural networks without training substitute models. In *ACM Workshop on Artificial Intelligence and Security*, pages 15–26, 2017.

[10] Minhao Cheng, Thong Le, Pin-Yu Chen, Huan Zhang, JinFeng Yi, and Cho-Jui Hsieh. Query-efficient hard-label black-box attack: an optimization-based approach. In *International Conference on Learning Representations*, pages 1–14, 2019.

[11] Minhao Cheng, Simranjit Singh, Pin-Yu Chen, Sijia Liu, and Cho-Jui Hsieh. Sign-OPT: a query-efficient hard-label adversarial attack. In *International Conference on Learning Representations*, pages 1–16, 2020.

[12] Shuyu Cheng, Yinpeng Dong, Tianyu Pang, Hang Su, and Jun Zhu. Improving black-box adversarial attacks with a transfer-based prior. In *Advances in Neural Information Processing Systems*, pages 10934–10944, 2019.

[13] Ekin D Cubuk, Barret Zoph, Dandelion Mane, Vijay Vasudevan, and Quoc V Le. AutoAugment: learning augmentation strategies from data. In *IEEE/CVF Conference on Computer Vision and Pattern Recognition*, pages 113–123, 2019.

[14] Jia Deng, Wei Dong, Richard Socher, Li-Jia Li, Kai Li, and Li Fei-Fei. ImageNet: a large-scale hierarchical image database. In *IEEE Conference on Computer Vision and Pattern Recognition*, pages 248–255, 2009.

[15] Xuanyi Dong and Yi Yang. Searching for a robust neural architecture in four GPU hours. In *IEEE/CVF Conference on Computer Vision and Pattern Recognition*, pages 1761–1770, 2019.

[16] Yinpeng Dong, Hang Su, Baoyuan Wu, Zhifeng Li, Wei Liu, Tong Zhang, and Jun Zhu. Efficient decision-based black-box adversarial attacks on face recognition. In *IEEE/CVF Conference on Computer Vision and Pattern Recognition*, pages 7714–7722, 2019.

[17] Alhussein Fawzi, Seyed-Mohsen Moosavi-Dezfooli, and Pascal Frossard. Robustness of classifiers: from adversarial to random noise. In *Advances in Neural Information Processing Systems*, page 1632–1640, 2016.

[18] Chuan Guo, Mayank Rana, Moustapha Cisse, and Laurens van der Maaten. Countering adversarial images using input transformations. In *International Conference on Learning Representations*, pages 1–12, 2018.

[19] Dongyoon Han, Jiwhan Kim, and Junmo Kim. Deep pyramidal residual networks. In *IEEE Conference on Computer Vision and Pattern Recognition*, pages 5927–5935, 2017.

[20] Kaiming He, Xiangyu Zhang, Shaoqing Ren, and Jian Sun. Deep residual learning for image recognition. In *IEEE Conference on Computer Vision and Pattern Recognition*, pages 770–778, 2016.

[21] Jie Hu, Li Shen, and Gang Sun. Squeeze-and-excitation networks. In *IEEE/CVF Conference on Computer Vision and Pattern Recognition*, pages 7132–7141, 2018.

[22] Andrew Ilyas, Logan Engstrom, and Aleksander Madry. Prior convictions: black-box adversarial attacks with bandits and priors. In *International Conference on Learning Representations*, pages 1–25, 2019.

[23] Alex Krizhevsky. Learning multiple layers of features from tiny images. pages 1–60, 2009.

[24] Huichen Li, Xiaojun Xu, Xiaolu Zhang, Shuang Yang, and Bo Li. QEBA: Query-efficient boundary-based blackbox attack. In *IEEE/CVF Conference on Computer Vision and Pattern Recognition*, pages 1221–1230, 2020.

[25] Yanpei Liu, Xinyun Chen, Chang Liu, and Dawn Song. Delving into transferable adversarial examples and black-box attacks. In *International Conference on Learning Representations*, pages 1–24, 2017.

[26] Yujia Liu, Seyed-Mohsen Moosavi-Dezfooli, and Pascal Frossard. A geometry-inspired decision-based attack. In *IEEE/CVF International Conference on Computer Vision*, pages 4889–4897, 2019.

[27] Zihao Liu, Qi Liu, Tao Liu, Nuo Xu, Xue Lin, Yanzhi Wang, and Wujie Wen. Feature distillation: DNN-oriented jpeg compression against adversarial examples. In *IEEE/CVF Conference on Computer Vision and Pattern Recognition*, pages 860–868, 2019.

[28] Chen Ma, Li Chen, and Jun-Hai Yong. Simulating unknown target models for query-efficient black-box attacks. In *IEEE/CVF Conference on Computer Vision and Pattern Recognition*, pages 11835–11844, 2021.

[29] Aleksander Madry, Aleksandar Makelov, Ludwig Schmidt, Dimitris Tsipras, and Adrian Vladu. Towards deep learning models resistant to adversarial attacks. In *International Conference on Learning Representations*, pages 1–28, 2018.

[30] Thibault Maho, Teddy Furon, and Erwan Le Merrer. SurFree: a fast surrogate-free black-box attack. In *IEEE/CVF Conference on Computer Vision and Pattern Recognition*, pages 10430–10439, 2021.

[31] Seungyong Moon, Gaon An, and Hyun Oh Song. Parsimonious black-box adversarial attacks via efficient combinatorial optimization. In *International Conference on Machine Learning*, pages 4636–4645, 2019.

[32] Seyed-Mohsen Moosavi-Dezfooli, Alhussein Fawzi, and Pascal Frossard. DeepFool: a simple and accurate method to fool deep neural networks. In *IEEE Conference on Computer Vision and Pattern Recognition*, pages 2574–2582, 2016.

[33] Ali Rahmati, Seyed-Mohsen Moosavi-Dezfooli, Pascal Frossard, and Huaiyu Dai. GeoDA: a geometric framework for black-box adversarial attacks. In *IEEE/CVF Conference on Computer Vision and Pattern Recognition*, pages 8446–8455, 2020.

[34] Yucheng Shi, Yahong Han, and Qi Tian. Polishing decision-based adversarial noise with a customized sampling. In *IEEE/CVF Conference on Computer Vision and Pattern Recognition*, pages 1030–1038, 2020.

[35] Christian Szegedy, Sergey Ioffe, Vincent Vanhoucke, and Alexander Alemi. Inception-v4, inception-resnet and the impact of residual connections on learning. In *AAAI Conference on Artificial Intelligence*, page 4278–4284, 2017.

[36] Christian Szegedy, Vincent Vanhoucke, Sergey Ioffe, Jon Shlens, and Zbigniew Wojna. Rethinking the inception architecture for computer vision. In *IEEE Conference on Computer Vision and Pattern Recognition*, pages 2818–2826, 2016.

[37] Xin Wang, Jie Ren, Shuyun Lin, Xiangming Zhu, Yisen Wang, and Quanshi Zhang. A unified approach to interpreting and boosting adversarial transferability. In *International Conference on Learning Representations*, pages 1–35, 2021.

[38] Dongxian Wu, Yisen Wang, Shu-Tao Xia, James Bailey, and Xingjun Ma. Skip connections matter: on the transferability of adversarial examples generated with ResNets. In *International Conference on Learning Representations*, pages 1–15, 2020.

[39] Yoshihiro Yamada, Masakazu Iwamura, Takuya Akiba, and Koichi Kise. Shakedrop regularization for deep residual learning. *IEEE Access*, 7:186126–186136, 2019.

[40] Ziang Yan, Yiwen Guo, Jian Liang, and Changshui Zhang. Policy-driven attack: learning to query for hard-label black-box adversarial examples. In *International Conference on Learning Representations*, pages 1–15, 2021.

[41] Sergey Zagoruyko and Nikos Komodakis. Wide residual networks. In *British Machine Vision Conference*, pages 87.1–87.12, 2016.

[42] Hongyang Zhang, Yaodong Yu, Jiantao Jiao, Eric Xing, Laurent El Ghaoui, and Michael Jordan. Theoretically principled trade-off between robustness and accuracy. In *International Conference on Machine Learning*, pages 7472–7482, 2019.

[43] Jingfeng Zhang, Jianing Zhu, Gang Niu, Bo Han, Masashi Sugiyama, and Mohan Kankanhalli. Geometry-aware instance-reweighted adversarial training. In *International Conference on Learning Representations*, pages 1–29, 2021.